ACS APPLIED MATERIALS & INTERFACES

Research Article

www.acsami.org

Spray-Deposition and Photopolymerization of Organic–Inorganic Thiol–ene Resins for Fabrication of Superamphiphobic Surfaces

Li Xiong,[†] Laken L. Kendrick,[†] Hannele Heusser,[†] Jamie C. Webb,[†] Bradley J. Sparks,[†] James T. Goetz,[†] Wei Guo,[†] Christopher M. Stafford,[‡] Michael D. Blanton,[†] Sergei Nazarenko,[†] and Derek L. Patton*[,†]

[†]School of Polymers and High Performance Materials, University of Southern Mississippi, Hattiesburg, Mississippi 39406, United States

[‡]Materials Measurement Laboratory, National Institute of Standards and Technology, Gaithersburg, Maryland 20899, United States

Supporting Information

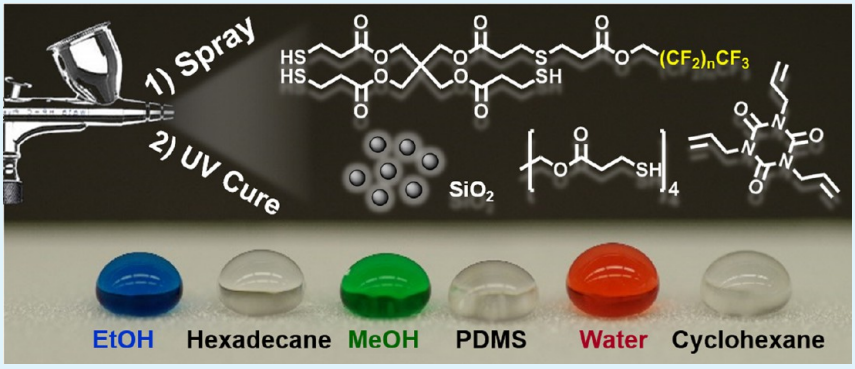

ABSTRACT: Superamphiphobic surfaces, exhibiting high contact angles and low contact angle hysteresis to both water and low surface tension liquids, have attracted a great deal attention in recent years because of the potential of these materials in practical applications such as liquid-resistant textiles, self-cleaning surfaces, and antifouling/anticorrosion coatings. In this work, we present a simple strategy for fabricating of superamphiphobic coatings based on photopolymerization of hybrid thiol–ene resins. Spray-deposition and UV photopolymerization of thiol–ene resins containing hydrophobic silica nanoparticles and perfluorinated thiols provide a multiscale topography and low-energy surface that endows the surface with superamphiphobicity. The wettability and chemical composition of the surfaces were characterized by contact-angle goniometry and X-ray photoelectron spectroscopy, respectively. The hierarchical roughness features of the thiol–ene surfaces were investigated with field-emission scanning electron microscopy. Droplet impact and sandpaper abrasion tests indicate the coatings respectively possess a robust antiwetting behavior and good mechanical durability.

KEYWORDS: *superamphiphobic, superoleophobic, photopolymerization, thiol–ene, bioinspired, spray-deposited*

1. INTRODUCTION

Tailoring of solid–liquid interfacial interactions, such as wettability, is a subject of paramount importance in materials research and offers broad reaching implications for a variety of everyday and technological applications.[1] Nature offers many awe-inspiring examples of engineered interfaces designed to minimize solid–liquid interfacial interactions resulting in the antiwetting behavior illustrated by observing water drops on the surface of the Lotus leaf[2] or on the skin of the European Giant Springtail.[3,4] These natural surfaces are fascinating examples of superhydrophobic wetting—wherein the surface exhibits an apparent water contact angle greater than 150°, contact angle hysteresis less than 10°, and low roll-off angles. It is now well-established that the superhydrophobic wetting state can be attributed to both chemical composition (typically low surface energy constituents) and geometric parameters (typically hierarchical roughness) of the solid interface. The hierarchical roughness serves to either increase or decrease the contact area of the solid–liquid interface resulting in a so-called apparent contact angle. The liquid either completely conforms to the surface roughness to increase the solid–liquid contact area—an adhesive wetting behavior described as the Wenzel[5] wetting state, or the liquid bridges between surface roughness protrusions creating a composite solid–liquid–air interface—a wetting behavior denoted as the Cassie–Baxter[6] wetting state. Biomimetic design of artificial interfaces targeting the Cassie–Baxter wetting state has led to a better understanding of the underlying wetting mechanisms and to the exploitation of this antiwetting phenomenon for a variety of applications including water-resistant textiles, antifouling/anticorrosion/antifogging coatings, and oil–water separations.[7−10]

Received: May 2, 2014
Accepted: June 9, 2014
Published: June 9, 2014

Although nature offers many design protocols for superhydrophobic surfaces, the path to superamphiphobicity—surfaces that are antiwetting (water and oil contact angles >150°; contact angle hysteresis <10°) in contact with both high and low surface tension liquids—is less defined. Relatively few examples of naturally superamphiphobic materials have been reported with the exception of bacterial (*Bacillus subtilis*) biofilm colonies reported by Aizenberg et al.[11] and springtails (*Orthonychiurus stachianus* and *Tetrodontophora bielanensis*) reported by Werner et al.[4,12] Engineering superamphiphobic surfaces is more challenging because of the low surface tension of most organic liquids (i.e., hexadecane, λ_{lv} = 27.6 mN/m), which leads to contact angles less than 90° even on inherently hydrophobic, and "oil-resistant" surfaces (i.e., $\theta_{hexadecance}$ = 40° for PTFE).[13] Thus, in addition to the hierarchically rough surface with low surface energy required for superhydrophobicity, superamphiphobicity additionally requires a re-entrant, convex, or overhanging surface curvature to prevent low surface tension liquids from penetrating the surface protrusions and displacing the trapped air cushion, as first described by Tuteja and co-workers.[14,15] Since the seminal work of Tuteja, numerous approaches have been reported for the fabrication of superoleophobic or superamphiphobic surfaces,[16−19] including lithography,[14,20] sacrificial templating,[21,22] replication,[23,24] electrospinning,[25] particle/nanoparticle deposition,[26,27] sintering,[28] vapor deposition,[29,30] chemical etching,[31] sol−gel/aerogels,[32,33] and spray-deposition techniques.[34−41] With the exception of the lithographic approaches, most of the fabrication techniques mentioned rely on the random, multiscale nature of the surface protrusions to generate the overhanging surface curvature necessary to support the Cassie wetting state for low surface tension fluids.

The spray-deposition techniques, in particular, provide a simple and industrially viable approach for the fabrication of coatings with hierarchically structured surface morphologies over large surface areas. Steele et al.[34] demonstrated one of the earliest examples of spray-deposited superamphiphobic surfaces by atomizing a blend of ZnO nanoparticles with a waterborne perfluoroacrylate polymer emulsion. The nanocomposite coatings reported by Steele displayed high oil contact angles (154°) and low hysteresis values (6°). In similar approaches, Srinivasan et al.[36] and Campos et al.[39] spray deposited 1H,1H,2H,2H-heptadecafluorodecyl polyhedral oligomeric silsesquioxane/PMMA and fluoroalkylated-silica/fluoropolymer composite thin films, respectively, with both systems exhibiting good superamphiphobic properties. More recently, Ge et al.[40] reported the spray deposition of 1H,1H,2H,2H-perfluorooctyl functionalized silica with a poly(vinylidene fluoride-hexafluoropropylene) binder, and demonstrated superamphiphobicity and anticorrosion properties of the coating on copper substrates. These examples of spray-deposited superamphiphobic coatings clearly illustrate the simplicity in the fabrication approach, but rely only on coalescence of the polymer binder and nanoparticle fillers for film stabilization—an approach that likely leads to subpar thermal and mechanical durability of the delicate surface structure (such data was not reported in the examples cited). Although unexplored specifically in spray-deposited superamphiphobic coatings, cross-linking the polymeric binder has been shown to improve mechanical durability of superamphiphobic coatings fabricated using other deposition techniques (i.e., spin coating).[42] In previous work, we demonstrated spray-deposition and photopolymerization of hybrid inorganic−organic thiol−ene resins as a simple route to generate superhydrophobic coatings.[43] The spray process provided a hierarchically structured surface that could be stabilized by cross-linking the resin via thiol−ene photopolymerization. The simplicity of the fabrication process enabled the production of superhydrophobic coatings on a variety of substrates; however, these coatings were oleophilic because of the incorporation of siloxane monomer constituents in the coating formulation.[43]

In the present work, we expand the simple approach of spray-deposition and photopolymerization of hybrid inorganic−organic thiol−ene resins to target coatings with superamphiphobic wetting properties. Superamphiphobicity is achieved by introducing a fluorinated multifunctional thiol into the thiol−ene formulation to significantly lower the surface tension of the resin. It is expected that the fluorinated thiol constituents will segregate to the surface of the coating upon spray deposition, and that these molecules will be immobilized, or locked into place at the surface of the coating upon photopolymerization. The thiol−ene resins are formulated in an organic solvent using a multifunctional alkene, trimethylsilyl-modified silica nanoparticles for nanoscale roughness, and a combination of the fluorinated and nonfluorinated multifunctional thiols as low surface tension components. Spray-deposition and photopolymerization of this formulation results in a hierarchically structured morphology where the morphology, and ultimately the wetting properties, are dependent on the nanoparticle loading level and the concentration of fluorinated thiol. In addition to evaluation and discussion of wetting properties using water and hexadecane as probes, the chemical, thermal, and mechanical durability of the composite coatings are discussed.

2. EXPERIMENTAL SECTION

2.1. Materials. All reagents were obtained at the highest purity available and used without further purification unless otherwise specified. Tetrahydrofuran (THF), 1,3,5-triallyl-1,3,5-triazine-2,4,6 (1H, 3H, 5H) trione (TTT), and 2,2-dimethoxy-2-phenylacetophenone (DMPA) were obtained from Sigma-Aldrich. Pentaerythritol tetra(3-mercaptopropionate) (PETMP) was obtained from Bruno Bock. Aerosil R972, a trimethylsilyl $-Si(CH_3)_3$ surface functionalization fumed silica with an average primary particle size of 16 nm, was kindly donated as product samples by Evonik Industries. Perfluorinated acrylates 1H,-1H-perfluoro-n-decyl acrylate and 1H,-1H-perfluoroheptyl acrylate were purchased from Exfluor Research Corporation. Fluorinated multifunctional thiols were synthesized using a thiol-Michael reaction between PETMP and perfluorinated acrylates following a synthetic procedure established by Shin and coworkers[44] and extended to perfluorinated materials by Goetz et al.[45]

2.2. Characterization. Static and dynamic water contact angle measurements were performed using a Rame-Hart 200−00 Std.-Tilting B. goniometer. Static contact angles were measured using 6 μL water droplets, and the average of three measurements was reported. Dynamic contact angles were obtained by taking 10 measurements/s for 15 s of an advancing or receding water droplet using a syringe pump to dispense and withdraw water from the droplet on the surface at 0.15 mL/min. The roll off angle of a 6 μL drop was measured using the tilting feature of the goniometer. ImageJ Drop Analysis software was used to analyze the droplets and determine static and dynamic contact angle values. Surface free energy of samples without roughness was obtained using a Rame-Hart tensiometer with water and hexadecane as probe liquids according to the Fowkes two component model.[46] High speed video was recorded using a Phantom, version 5.1 (Vision Research, Inc., Wayne, NJ). Scanning electron microscopy (SEM) images were obtained using an FEI Quanta 200 SEM at 25 kV under high vacuum conditions. High resolution field-emission SEM (FE-SEM) images were obtained with a Zeiss Sigma VP FEG-SEM at

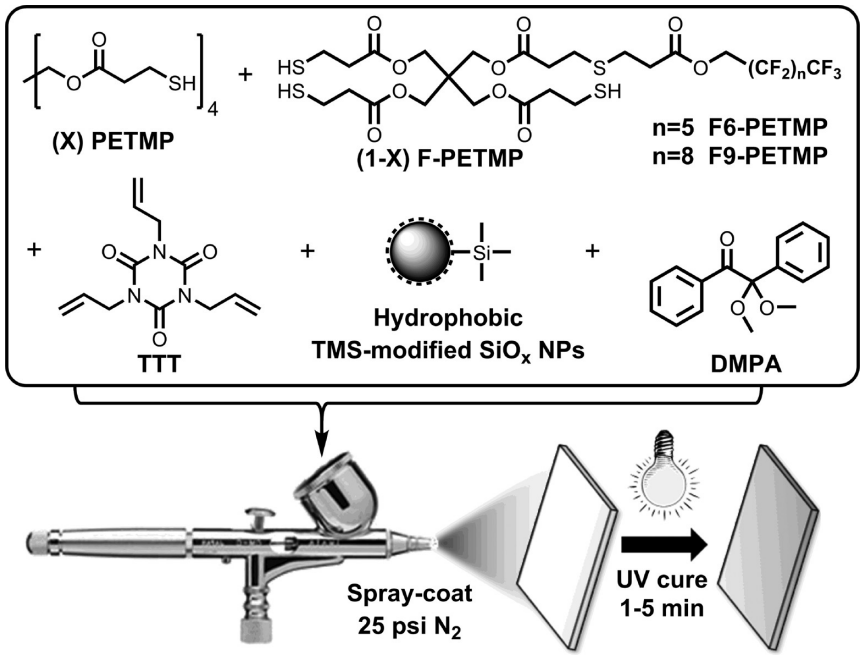

Figure 1. Schematic of the spray-deposition and photopolymerization process using hybrid inorganic–organic thiol–ene resins laden with hydrophobic silica nanoparticles.

10 kV in high vacuum mode. XPS measurements were performed using a Kratos Axis Ultra Spectrometer (Kratos Analytical, Manchester, UK) with a monochromatic Al K X-ray source (1486.6 eV) operating at 140 W under 1.0×10^{-9} Torr. Measurements were performed in hybrid mode using electrostatic and magnetic lenses, and the pass energy of the analyzer was set at 20 eV for high-resolution spectra and 160 eV for survey scans, with energy resolutions of 0.1 and 0.5 eV, respectively. Generally, total acquisition times of 180 and 440 s were used to obtain high resolution and survey spectra, respectively. For a 0° take off angle (angle between sample surface normal and the electron optical axis of the spectrometer), the maximum information depth of the measurements was approximately 8–10 nm.[47] All XPS spectra were recorded using the Kratos Vision II software; data files were translated to VAMAS format and processed using the CasaXPS software package (v. 2.3.12). Binding energies were calibrated with respect to C 1s at 284.8 eV. Following application of a Shirley background subtraction, atomic percentages were calculated from the elemental peak areas present in the survey spectra using the relative sensitivity factors provided by Kratos. High resolution spectra were fitted using mixtures of Gaussian/Lorentzian peaks after a Shirley background subtraction. The fitting parameters included peak position, full width at half-maximum, intensity, and the Guassian fraction. Abrasion resistance of the films was evaluated using a reciprocating abrasion test similar to methods reported in literature.[48] Drop impact testing was carried out according to literature methods.[21] A schematic of the abrasion test and the drop impact test (Figure S1) can be found in the Supporting Information.

2.3. Film Preparation. Thiol–ene resins were prepared by weighing out the desired ratio of fluorinated (F_nPETMP) and nonfluorinated (PETMP) multifunctional thiols, alkene, and photoinitiator into a glass jar, maintaining a 1:1 stoichiometric ratio of thiol to alkene. The mass ratio of F_nPETMP/PETMP was varied at 0:100, 10:90, 20:80, and 30:70. A specified amount of hydrophobic silica nanoparticles (Aerosil R972 = 0, 10, 20, 30 wt % relative to resin) was added to the resin mixture and subsequently dispersed in THF (15:1 w/w solvent/resin) by ultrasonication for 30–60 min. Glass slides and aluminum Q-panels were used as model substrates. An air brush with a nozzle diameter of 0.635 mm (Paasch H#3 obtained from McMaster Carr) was connected to a compressed nitrogen source (25 psi) and used to spray coat the thiol–ene resin onto the substrates at a distance of 15 cm and a rate of 2 mL/min. The coated substrates were allowed to sit for 1 min and subsequently cured under a UV flood lamp (16 mW/cm^2) for 5 min.

3. RESULTS AND DISCUSSION

3.1. Resin Formulation and Film Fabrication. As shown in Figure 1, thiol–ene photopolymer resins were formulated with a photoinitiator (DMPA), a trifunctional alkene (TTT), a mixture of multifunctional thiols (PETMP and F_nPETMP), and hydrophobic trimethysilyl-modified silica nanoparticles (TMS-SiO_2). TMS-SiO_2 was incorporated at 10%, 20%, and 30% by weight relative to the total weight of the thiol–ene resin. Two perfluorinated chain lengths were investigated as modifiers for PETMP, including 1H,-1H-perfluoroheptyl (six fluorinated carbons, F_6PETMP) and 1H,-1H-perfluoro-n-decyl (nine fluorinated carbons, F_9PETMP). The fluorinated multifunctional F_nPETMP thiols were incorporated to significantly lower the surface energy of the thiol–ene resin, with the 1H,-1H--perfluoroheptyl version of interest because of the reduced environmental persistence of perfluorinated materials with shorter chain lengths. F_6PETMP and F_9PETMP were incorporated at 10 and 30 wt % relative to the total weight of the thiol components (i.e., PETMP + F-PETMP), while maintaining a 1:1 molar ratio between total thiol and alkene functional groups. Attempts to use pure F_6PETMP or F_9PETMP as the thiol constituent in the formulation, as well as concentrations of F_6PETMP or F_9PETMP higher than 30 wt % resulted in deteriorated film forming properties. To help simplify the notation for each system, we will represent the various formulations as F_nPETMP(x)/SiO_2(y), where n represents either 6 or 9 fluorinated carbons, and x and y represent the wt % F_nPETMP and wt % TMS-SiO_2, respectively.

To formulate the resins, we diluted the TMS-SiO_2 nanoparticles into THF and dispersed using probe ultrasonication. The remaining resin components were then dissolved into the nanoparticle dispersion, mixed thoroughly, and spray-coated onto glass and aluminum substrates using a

simple air-brush device. The spray-coating process atomizes the resin solution into a random distribution of micrometer and submicrometer-sized droplets and directs these droplets toward the substrate with air flow. Adjustment of the spray-coating parameters (i.e., nozzle to substrate distance, sweep speed, nozzle size, air pressure, etc.) enables the deposition of films ranging from a "dry-sprayed" layer to a fully wet layer, where rapid volatilization of the organic solvent from the microparticles prior to or upon deposition results in the formation of a corpuscular, microstructured morphology. The importance of spray-coating parameters on the wetting and wear behavior of superhydrophobic surfaces was recently reported by Yeong et al.[49] In the current work, deposition of films under "dry-spray" conditions resulted in chalky textures, thus such conditions were avoided because of the fragile nature of the resulting morphologies (i.e., surfaces were easily damaged upon handling). The combination of TMS-modified SiO_2 nanoparticles with the microparticles from the spray process endow the surface with the desired hierarchical, or multiscale morphology necessary to achieve extreme antiwetting properties of the coatings. After allowing the solvent to evaporate from the deposited film for 1 min, the films were cured under a UV light in ambient atmosphere via thiol−ene photopolymerization. The photopolymerization process served to cross-link the thiol−ene polymer matrix and stabilize the multiscale morphology of the film. Upon optimization of the spray-coating process, the parameters associated with the spray deposition were kept constant as described in the Experimental Section. It is worth noting that the entire film fabrication process (from formulation to photopolymerization) can be completed in under 70 min, where the rate limiting step is the ultrasonic dispersion of nanoparticles.

3.2. Surface Morphology and Chemical Composition.

To achieve superamphiphobic wetting, surfaces must exhibit both a low interfacial energy and a re-entrant (or overhanging) surface morphology. The surface morphology of the spray-coated and photocured thiol−ene films was investigated using SEM. For comparison, SEM images of films formulated with nonfluorinated PETMP at various concentrations of TMS-SiO_2 nanoparticles are shown in Figure S2 in the Supporting Information. Figure 2a−c and d−f show a series of low-magnification SEM images for F_9PETMP(10) and F_9PETMP-(30) containing 10, 20, and 30% by weight TMS-SiO_2, respectively. Initial observations indicate that the concentration of F_9PETMP (10 versus 30%) plays a minimal role in altering the film morphology, while morphology is significantly dependent on the TMS-SiO_2 nanoparticle concentration. At 10% TMS-SiO_2 loading, the surface of the films exhibit a course morphology with low porosity on the micrometer scale (Figure 2a, d). This course morphology is likely attributed to the aggregation and coalescence of micrometer sized droplets formed during the spray deposition process. As the TMS-SiO_2 content is increased, the surface morphology of films containing 20% (Figure 2b, e) and 30% (Figure 2c, f) TMS-SiO_2 transition to a raspberry-like microstructure with high porosity resulting from the random agglomeration and deposition of spherical droplets during spray process. High-magnification FE-SEM images of the F_9PETMP(30)/SiO_2(30) film, shown in Figure 3a−c, confirm the presence of an agglomerated raspberry-like morphology, and further reveal the hierarchical nature of the surface roughness. Panels b and c in Figure 3 clearly show the multiscale structure with sub-100 nm TMS-SiO_2 nanoparticle aggregates superimposed over the surface of the larger sphere-like microparticles. More importantly, the hierarchical structures create protrusions with overhanging geometries at multiple scales capable of trapping air at the interface essential for superamphiphobicity.

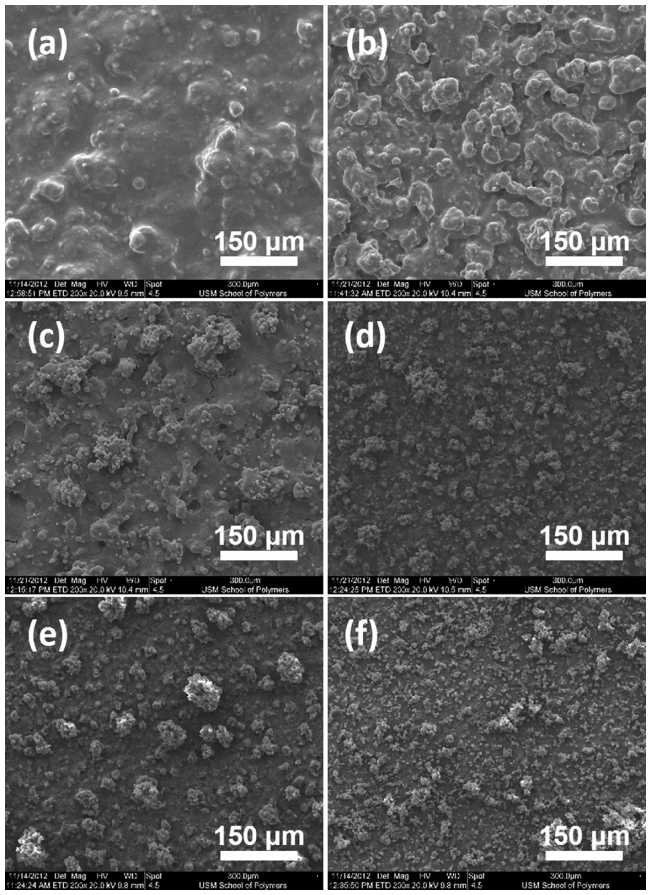

Figure 2. SEM micrographs of F_9PETMP(10) with (a) 10, (b) 20, and (c) 30% TMS-SiO_2 nanoparticles and F_9PETMP(30) with (d) 10, (e) 20, (f) and 30% TMS-SiO_2 nanoparticles.

Along with surface morphology, the chemical composition of the interface plays an important role in dictating the wetting properties of the photocured thiol−ene films. The low-surface-energy components within our formulation, i.e., F_6PETMP or F_9PETMP, experience a thermodynamic driving force to move toward the solid−air interface in order to minimize the solid−vapor interfacial free energy of the coatings.[50,51] The presence of solvent at the beginning of the spray deposition process ensures mobility of F_nPETMP, which should facilitate surface segregation. X-ray photoelectron spectroscopy was employed to probe the local chemical composition of the surface and the degree of surface segregation of the photocured coating (~8−10 nm probe depth).[47] Figure 4a−c shows the survey spectra for F_9PETMP(30)/SiO_2(0), F_9PETMP(30)/SiO_2(10), and F_9PETMP(30)/SiO_2(30), respectively; whereas the survey spectra for the F_9PETMP(10) series can be found in the Supporting Information (Figure S3). The spectra for the F_9PETMP(30)/SiO_2(0) and F_9PETMP(30)/SiO_2(10) samples exhibit peaks at 162.8, 284.8, 399.8, 531.8, and 687.8 eV corresponding to the binding energies for the S 2p, C 1s, N 1s, O 1s, and F 1s, respectively. It is interesting to note that peaks attributable to the TMS-modified SiO_2 nanoparticles (i.e., Si 2p, Si 2s) are not observed in the survey spectrum for the F_9PETMP(30)/SiO_2(10) sample; however, the Si 2p and Si 2s

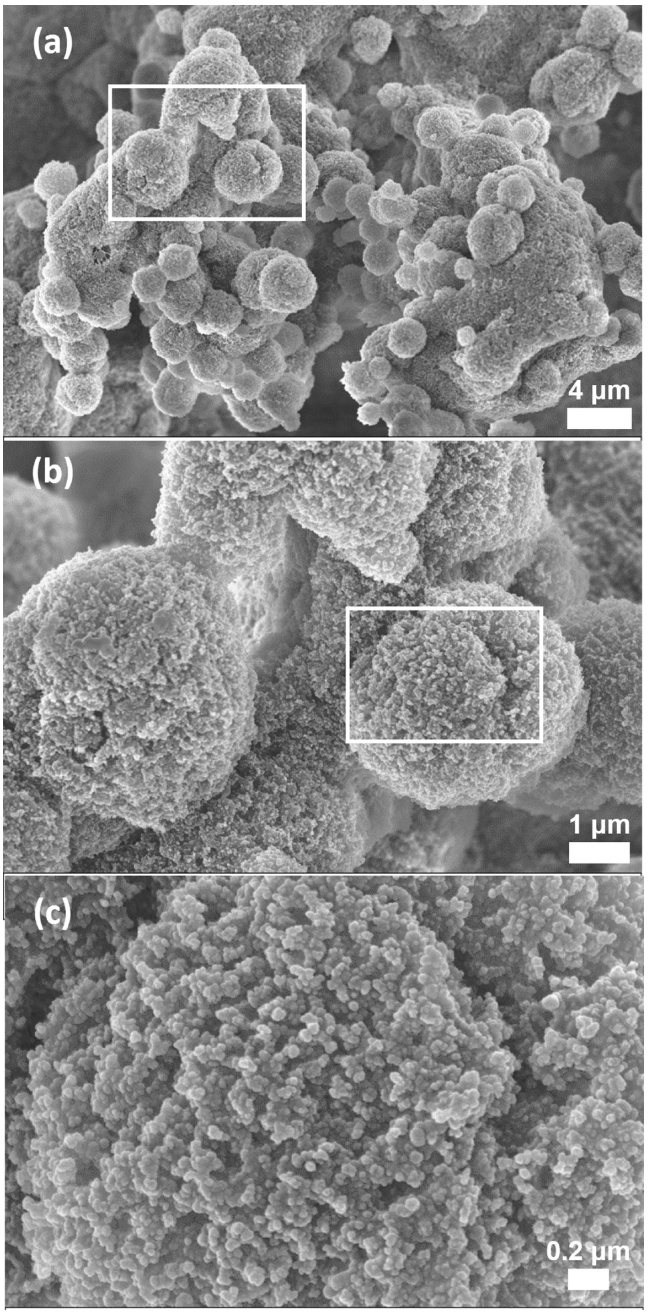

Figure 3. High-resolution FE-SEM micrographs of F_9PETMP(30)/SiO_2(30) at (a) 2800×, (b) 10 000×, and (c) 32 000× magnification.

peaks at 102.8 and 153.9 eV are clearly present in the survey spectrum for the F_9PETMP(30)/SiO_2(30). This observation suggests that the TMS-SiO_2 nanoparticles are predominately covered by thiol−ene resin at low nanoparticle loading levels, and are at least partially exposed at the interface at higher loading levels. Additionally, atomic compositions obtained by XPS were used to quantify the surface segregation of F_nPETMP by comparing experimentally observed atomic ratios−specifically the F/C ratio−with atomic ratios calculated from the bulk resin composition. The F/C ratios calculated from the bulk compositions for F_9PETMP(10)/SiO_2(0) and F_9PETMP(30)/SiO_2(0) are 0.028 and 0.091, respectively, as shown in Table 1. The enhanced F/C ratios obtained from the survey spectra for the F_9PETMP(10)/SiO_2(0) (F/C = 0.419 ± 0.015) and F_9PETMP(30)/SiO_2(0) (F/C = 0.521 ± 0.016) samples

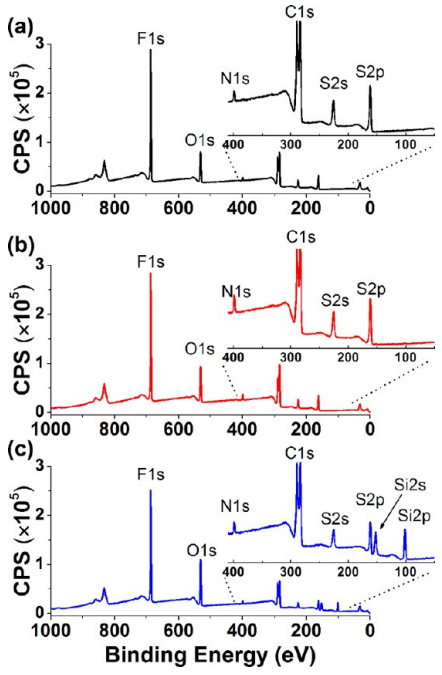

Figure 4. XPS survey spectra for F_9PETMP(30) films containing (a) 0, (b) 10, and (c) 30% TMS-SiO_2 nanoparticles. The insets show a zoomed region of each spectrum from 50−410 eV.

Table 1. Surface Composition of Sprayed F_9PETMP−PETMP-TTT Hybrid Inorganic−Organic Thiol−ene Films

sample	F/C calcd[a]	F/C obsvd (XPS)
F_9PETMP(10)/SiO_2(0)	0.028	0.419 ± 0.015
F_9PETMP(10)/SiO_2(10)	[b]	0.499 ± 0.016
F_9PETMP(10)/SiO_2(30)	[b]	0.559 ± 0.019
F_9PETMP(30)/SiO_2(0)	0.091	0.521 ± 0.016
F_9PETMP(30)/SiO_2(10)	[b]	0.479 ± 0.015
F_9PETMP(30)/SiO_2(30)	[b]	0.579 ± 0.013

[a]F/C ratio calculated according to the bulk composition and stoichiometry of the resin. [b]The same calculation was not possible in the presence of trimethylsilyl-modified silica nanoparticles.

confirm the surface enrichment of the low surface energy F_9PETMP component. Generally, slightly higher F/C values were observed with 10 and 30 wt % nanoparticles included in the formulation, which may be attributed to greater mobility of the resin components upon deposition because of the higher solvent content necessary to spray the nanoparticle-laden formulations. However, accounting for the amount of carbon present on the TMS-modified nanoparticles made calculating the comparative bulk atomic composition difficult with TMS-SiO_2 in the formulation, thus, bulk values were not determined for sample containing nanoparticles. Considering both the large surface roughness in our samples and the large difference in kinetic energy between the F 1s and C 1s photoelectrons that results in a significantly smaller sampling depth for fluorine than carbon, we use the F/C ratios only to show the tendency of F_nPETMP to segregate toward the film−air interface.

High-resolution XPS was also employed to provide additional insight into the chemical composition of the film interface. Figure 5a−d respectively shows the high-resolution C 1s spectra obtained from the F_9PETMP(10)/SiO_2(0), F_9PETMP(30)/SiO_2(0), F_9PETMP(10)/SiO_2(30), and F_9PETMP(30)/SiO_2(30) surfaces. The spectra were deconvo-

dx.doi.org/10.1021/am502691g | ACS Appl. Mater. Interfaces 2014, 6, 10763−10774

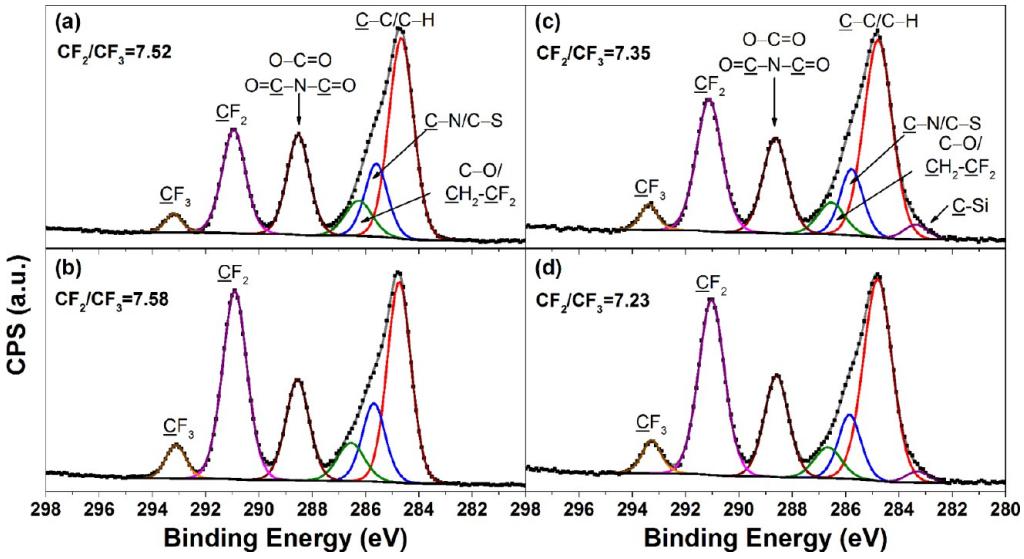

Figure 5. High-resolution C 1s spectra of (a) F_9PETMP(10)/SiO_2(0), (b) F_9PETMP(30)/SiO_2(0), (c) F_9PETMP(10)/SiO_2(30), and (d) F_9PETMP(30)/SiO_2(30) surfaces.

luted into six component peaks with binding energies characteristic of the molecular units comprising the polymer network, including −C−C/C−H (284.8 eV), −C−N/−C−S (285.7 eV), −C−O/−CH_2CF_2− (286.5 eV), −O−C═O/−O═C−N−C═O (288.6 eV), −CF_2 (290.9 eV), and −CF_3 (293.1 eV). F_9PETMP(10)/SiO_2(30) and F_9PETMP(30)/SiO_2(30) surfaces required an additional peak at 283.4 eV corresponding to the C−Si group arising from the presence of TMS-SiO_2 nanoparticles at the interface. Peak fits were summed together when significant overlap of the binding energies for specific molecular structures prevented unequivocal deconvolution (i.e., −C−N/−C−S, −C−O/−CH_2CF_2−, and −O−C═O/−O═C−N−C═O). Assignments of these components agree well with those reported for materials with similar molecular constituents.[52] The CF_2/CF_3 peak area ratio varied from 7.52−7.58 for surfaces without TMS-SiO_2 nanoparticles to 7.23−7.35 for surfaces containing 30 wt % TMS-SiO_2. In all cases, the CF_2/CF_3 ratio closely resembled the expected ratio of 8 (i.e., −CH_2−$(CF_2)_8$-CF_3), which along with the previously discussed XPS survey data confirms the interface is rich with perfluoro-n-decyl chains. Although chain orientation cannot be directly inferred from these XPS experiments, the presence of CF_3 groups is important and is known to play a prominent role in lowering the surface free energy of the films (discussed vide infra).[53,54]

3.3. Wetting Behavior. The wetting properties of the fabricated films were evaluated by measuring the static contact angle (CA), dynamic contact angle, contact angle hysteresis, and roll off angle using both high- and low-surface-tension liquids, including water (γ_{LV} = 72.3 mN/m) and n-hexadecane (γ_{LV} = 27.6 mN/m). Table 2 summarizes the wetting behavior of the flat (nontextured) thiol−ene films containing 10 and 30% of either F_6PETMP or F_9PETMP, but without the addition of TMS-SiO_2 nanoparticles. As shown, the static water CA (WCA) increased from 73° for the nonfluorinated PETMP(100)/SiO_2(0) film to 95 and 99° upon incorporation of 10 and 30 wt % F_6PETMP, respectively. Likewise, the nonfluorinated PETMP-TTT film was completely wetted by hexadecane, but exhibited an oil (hexadecane) contact angle (OCA) of 71 and 73°, respectively, with the addition of 10 and

Table 2. Wetting Properties of Nontextured F_nPETMP−PETMP-TTT Films without TMS-SiO_2 Nanoparticles

sample	θ_{water} (deg)	θ_{oil} (deg)[a]	surface energy (mN/m)[b]
PETMP(100)/SiO_2(0)	72.6 ± 0.9	0	
F_6PETMP(10)/SiO_2(0)	95.4 ± 1.5	71.3 ± 1.1	17.6 ± 0.65
F_6PETMP(30)/SiO_2(0)	99.3 ± 1.2	73.3 ± 3.2	15.7 ± 0.72
F_9PETMP(10)/SiO_2(0)	118 ± 0.8	81.5 ± 0.6	9.61 ± 0.16
F_9PETMP(30)/SiO_2(0)	119 ± 0.3	81.3 ± 0.1	9.59 ± 0.03

[a]Hexadecane. [b]Calculated according to the Fowkes two-component model.

30 wt % F_6PETMP. As expected, incorporation of F_9PETMP into the resin resulted in films with greater hydrophobicity (WCA, 118°) and oleophobicity (OCA, 81°) because of the longer fluorinated chain length, but showed a minimal dependence on the F_9PETMP concentration. This concentration independent wetting behavior is likely attributed to the saturation of the film interface with 1H,1H-perfluoro-n-decyl functional groups, as XPS showed large enhancements in the F/C ratio for both 10 and 30 wt % F_9PETMP. From these contact angle measurements, the calculated surface energy decreased from 17.6 mN/m for films containing 10 wt % F_6PETMP to 9.6 mN/m for films containing 10 or 30 wt % F_9PETMP. The wetting properties and surface energy values reported herein for films containing F_6PETMP and F_9PETMP are characteristic of films containing −CF_3 groups at the interface (as previously shown by XPS), and compare well with values reported in the literature for other thin films comprising similar perfluoro-*n*-alkyl acrylate derivatives.[50,54,55]

With an understanding of the wetting properties associated with F_nPETMP thiol−ene resins in nontextured films, we next investigated the wetting behavior of these resins containing TMS- SiO_2 nanoparticles. Figure 6 shows the relationship between the static WCA and TMS-SiO_2 nanoparticle loading level for both F_6PETMP and F_9PETMP resin systems following

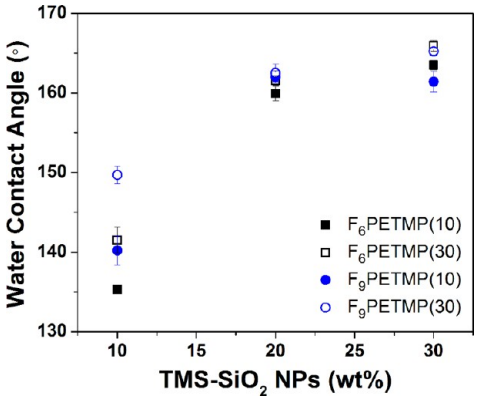

Figure 6. Variation in the static water contact angle as a function of TMS-SiO_2 nanoparticle loading level for samples formulated with F_6PETMP and F_9PETMP. The error bars represent one standard deviation of the data, which is taken as the uncertainty of the measurement.

spray deposition and photopolymerization. For films containing 10% TMS-SiO_2, the static WCA increased based on the fluorinated chain length (F_6 vs F_9) and concentration, with 10 wt % F_6PETMP exhibiting the lowest WCA of 135° and 30 wt % F_9PETMP exhibiting the highest WCA of 150°. Films containing 10% TMS-SiO_2 exhibited a Wenzel-type wetting behavior evident from the strong pinning of the water droplet during receding contact angle measurements and adhesion of the droplet during roll-off measurements. Films containing 20% and 30% TMS-SiO_2 all exhibit WCAs in the superhydrophobic regime (160−165°) with minimal dependence on the fluorinated PETMP chain length or concentration, as shown in Figure 6. These same films, as summarized in Table 3, also show relatively low contact angle hysteresis values (<7°) and low roll off angles (<8°) characteristic of a Cassie−Baxter wetting state. The F_9PETMP(30)/SiO_2(30) film provided the highest superhydrophobic wetting performance with a water contact angle of 165°, 1.2° contact angle hysteresis, and a 1° roll-off angle.

The oleophobic properties of the thiol−ene films, summarized in Table 4, were evaluated using hexadecane as a probe liquid. Figure 7 shows the relationship between the static OCA and the TMS-SiO_2 nanoparticle loading level for each of the F_6PETMP and F_9PETMP resin systems. As shown, all films containing 10% TMS-SiO_2 remain oleophilic (oil CA < 90°) regardless of the fluorinated chain length or concentration of the F-PETMP. The oleophilic nature of these surfaces can be attributed to the course roughness observed by SEM, and therefore lack of the hierarchical surface morphology (see SEM

Table 3. Water Contact Angle Data for Sprayed F_nPETMP−PETMP-TTT Hybrid Inorganic−Organic Thiol−ene Thin Films

SiO_2 (wt %)	θ_{Adv} (deg)	θ_{Static} (deg)	θ_{Rec} (deg)	θ_{Hys} (deg)	θ_{Roll} (deg)
		PETMP(100)/SiO_2(y)			
10	67.7 ± 1.6	59.5 ± 1.7			
20	108.2 ± 2.2	100.4 ± 2.8			
30	154.8 ± 1.3	152.9 ± 1.9	150.3 ± 2.4	4.5	8 ± 2
		F_6PETMP(10)/SiO_2(y)			
10	144.7 ± 0.8	135.3 ± 0.5			
20	163.9 ± 0.9	159.9 ± 0.9	156.7 ± 0.8	7.2	8 ± 1
30	164.7 ± 0.4	163.5 ± 0.6	159.3 ± 2.4	5.4	2 ± 1
		F_6PETMP(30)/SiO_2(y)			
10	149.6 ± 0.9	141.5 ± 1.6			
20	164.4 ± 0.3	161.5 ± 0.6	159.0 ± 0.8	5.4	6 ± 1
30	167.3 ± 0.3	165.9 ± 0.7	162.4 ± 0.5	4.9	1 ± 1
		F_9PETMP(10)/SiO_2(y)			
10	151.7 ± 1.2	140.2 ± 1.8			
20	162.9 ± 0.6	162.0 ± 0.8	159.3 ± 1.2	3.6	3 ± 1
30	162.3 ± 1.4	161.4 ± 1.3	160.7 ± 0.7	1.6	1 ± 1
		F_9PETMP(30)/SiO_2(y)			
10	154.5 ± 1.7	149.7 ± 1.1			
20	163.0 ± 1.0	162.5 ± 1.1	160.1 ± 0.8	2.9	2 ± 1
30	166.0 ± 1.0	165.2 ± 0.5	164.8 ± 0.8	1.2	1 ± 1

Table 4. Oil Contact Angle Data for Sprayed F-PETMP−PETMP-TTT Hybrid Inorganic−Organic Thiol−ene Thin Films

SiO_2 (wt %)	θ_{Adv} (deg)	θ_{Static} (deg)	θ_{Rec} (deg)	θ_{Hys} (deg)	θ_{Roll} (deg)
		PETMP(100)/SiO_2(y)			
10		0			
20		0			
30		0			
		F_6PETMP(10)/SiO_2(y)			
10	79.4 ± 2.0	70.9 ± 0.8			
20	146.9 ± 0.7	131.7 ± 2.9	89.7 ± 0.8	57.2	
30	151.0 ± 1.1	141.5 ± 1.3	121.3 ± 2.4	29.7	
		F_6PETMP(30)/SiO_2(y)			
10	80.6 ± 1.9	73.9 ± 1.6			
20	141.9 ± 0.9	135.4 ± 0.5	96.0 ± 0.8	45.9	
30	155.6 ± 1.4	153.1 ± 0.7	141.9 ± 0.9	13.7	7 ± 1
		F_9PETMP(10)/SiO_2(y)			
10	84.2 ± 0.9	81.2 ± 0.7	41.7 ± 1.8	42.5	
20	156.9 ± 0.6	147.4 ± 0.8	141.8 ± 0.7	15.1	
30	156.7 ± 1.1	151.2 ± 1.3	143.3 ± 1.7	13.4	
		F_9PETMP(30)/SiO_2(y)			
10	87.8 ± 0.7	86.7 ± 2.1	42.1 ± 1.9	45.7	
20	159.1 ± 0.7	153.3 ± 0.9	144.1 ± 0.8	15.0	7.5 ± 1
30	159.6 ± 0.8	155.3 ± 0.7	150.1 ± 1.3	9.5	4 ± 0.5

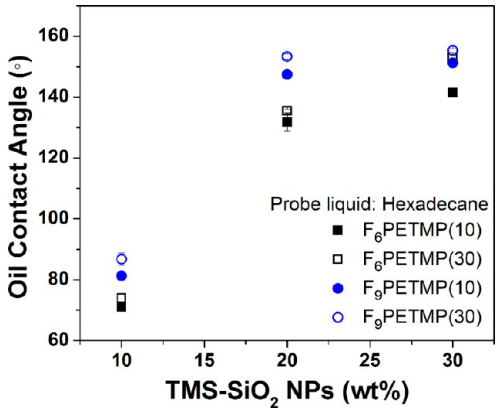

Figure 7. Variation in the static oil contact angle as a function of TMS-SiO_2 nanoparticle loading level for samples formulated with F_6PETMP and F_9PETMP. The error bars represent one standard deviation of the data, which is taken as the uncertainty of the measurement.

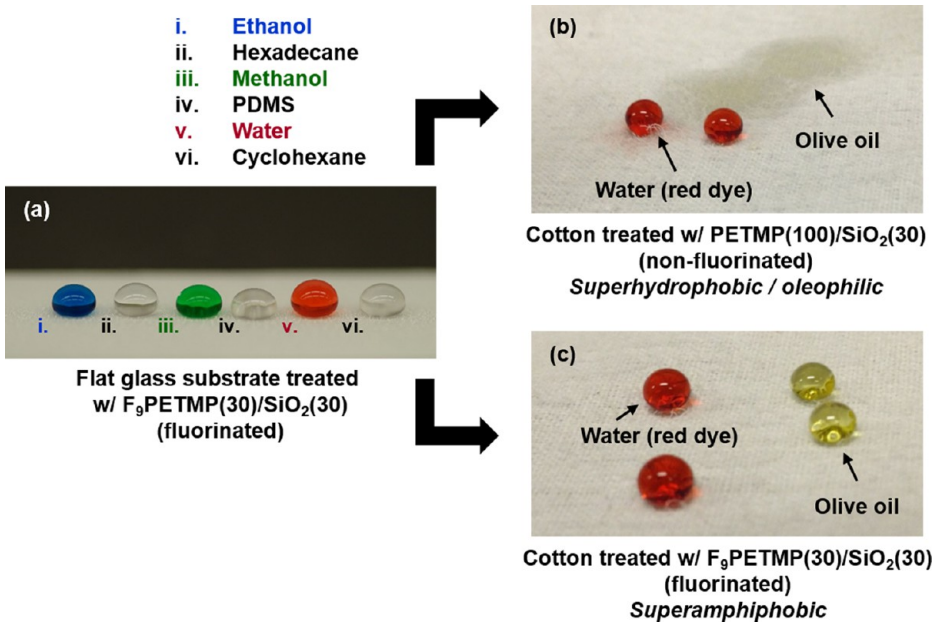

Figure 8. (a) Photograph of (left–right) ethanol, hexadecane, methanol, PDMS, water, and cyclohexane sitting on the surface of a F_9PETMP(30)/SiO_2(30) sample. Photograph of water and olive oil on a cotton textile treated with a (b) nonfluorinated PETMP(100)/SiO_2(30) and (c) F_9PETMP(30)/SiO_2(30).

images in Figure 2a, d) necessary to increase the contact angle with low surface tension liquids. At 20% TMS-SiO_2, we observed a sharp increase in the OCA for each film composition; however, only the F_9PETMP(30)/SiO_2(20) sample achieved the mark of superoleophobicity (oil CA 153°) albeit with a large hysteresis value (15°). Increasing the TMS-SiO_2 nanoparticle concentration to 30% enables the observation of superoleophobicity for a broader range of fluorinated chain lengths and concentrations including the F_6PETMP(30)/SiO_2(30), F_9PETMP(20)/SiO_2(30), and F_9PETMP(30)/SiO_2(30) film compositions. These three film compositions also exhibit relatively low hysteresis and roll off angles with hexadecane, with F_9PETMP(30)/SiO_2(30) showing the highest superoleophobicity (OCA 155°, θ_{Hys} 9.5°, and θ_{Roll} 4°). Referring back to Figure 3, we can relate the hierarchically structured agglomerates of raspberry-like particles to the re-entrant curvature or overhanging structure often cited in the literature as a critical requirement for superoleophobicity.[14,17] The combination of 30% TMS-SiO_2 and spray-coating process provides this type of overhanging, random structure, while sufficient fluorinated F_nPETMP concentrations provide a low surface energy material at the film interface. The observed trends in oleophobic wetting properties of our thiol–ene films highlight the more stringent interplay between intrinsic surface energy and surface structure necessary to achieve antiwetting with low-surface-tension liquids.

Figure 8a shows a photograph of several droplets sitting on the surface of a F_9PETMP(30)/SiO_2(30) sample, including ethanol (γ_{LV} = 22.1 mN/m), hexadecane (γ_{LV} = 27.6 mN/m), methanol (γ_{LV} = 22.7 mN/m), PDMS (γ_{LV} = 19 mN/m), water (γ_{LV} = 72.3 mN/m), and cyclohexane (γ_{LV} = 24.9 mN/m). For each liquid, the F_9PETMP(30)/SiO_2(30) surface showed a robust antiwetting interaction. The dynamic antiwetting behavior of the F_9PETMP(30)/SiO_2(30) coating with hexadecane and water dropped onto the surface can be viewed in videos provided in the Supporting Information. Panels b and c in Figure 8 show samples of cotton textile treated with PETMP(100)/SiO_2(30) (i.e., nonfluorinated) and F_9PETMP(30)/SiO_2(30), respectively. The nonfluorinated PETMP(100)/SiO_2(30) textile shows superhydrophobic wetting as evidenced by the red-dyed water droplet sitting on the surface, but exhibits an oleophilic wetting in contact with olive oil (γ_{LV} = 32.0 mN/m). Conversely, the cotton textile treated with F_9PETMP(30)/SiO_2(30) exhibits superamphiphobicity toward water and olive oil illustrating the important role F_9PETMP plays in the formulation.

3.4. Mechanical, Chemical, and Thermal Durability. Widespread implementation of antiwetting coatings in everyday applications (i.e., sporting equipment) and in advanced technological applications is arguably limited by issues associated with coating durability. The intricate, multiscale morphologies that give rise to unique wetting phenomena also give rise to mechanical fragility of the surface in response to abrasion. A number of excellent approaches have been reported that target improvements in mechanical damage and deformation (i.e., abrasion, peeling, stretching, etc.),[41,56–59] temperature stability,[60] and solvent resistance[61] of superhydrophobic surfaces, with fewer examples of mechanically robust superamphiphobic surfaces due to the more stringent requirements for overhanging surface morphology in the superamphiphobic regime.[15,21,25,32,33,42] In the current work, the mechanical robustness of the fabricated films was evaluated using a simple, lab-built reciprocating abrasion test. The film to be abraded was placed face up in contact with 2000 grit sandpaper. A loading pressure of 254 N/m^2 was applied and the loaded sandpaper was dragged across the sample in a reciprocating motion at a constant speed of 3.8 mm/s. The changes in water and oil contact angle as a function of the number of abrasion cycles (up to 350 cycles) for F_9PETMP(30)/SiO_2(30) films are shown in Figure 9a. As shown, the WCA decreases slightly with increasing number of abrasion cycles, but remains above 150°, and therefore superhydrophobic, after 200 abrasion cycles. The roll off angle increased from 1 ± 1° before abrasion to 14 ± 2° after 200 abrasion cycles,

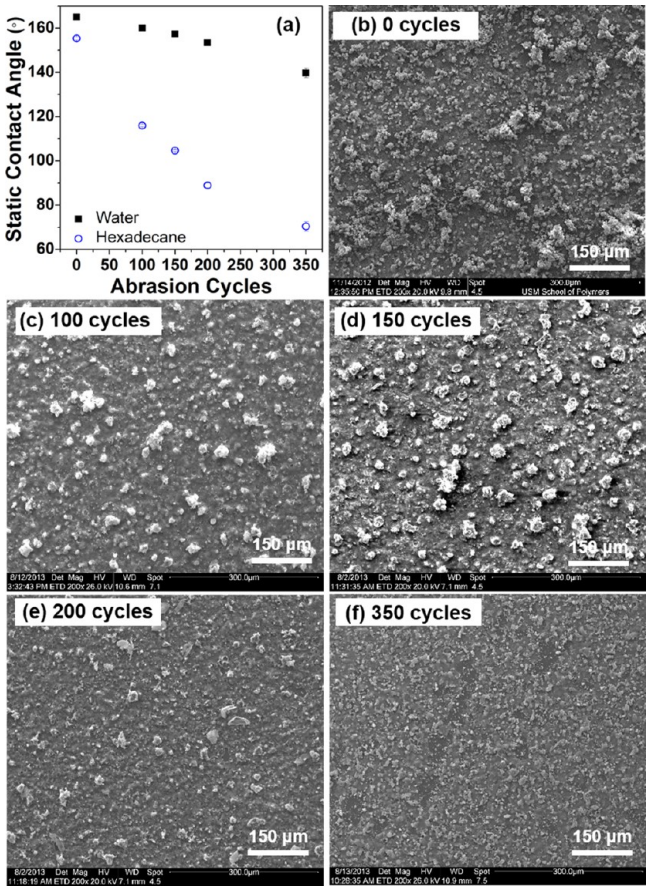

Figure 9. (a) Static water and oil (hexadecane) contact angles for F_9PETMP(30)/SiO_2(30) as a function of abrasion cycle. SEM images of the F_9PETMP(30)/SiO_2(30) surface following (b) 0, (c) 100, (d) 150, (e) 200, and (f) 350 abrasion cycles.

indicating the retention of good antiwetting properties toward water. After 350 abrasion cycles, the WCA dropped below 150° and the resulting surface exhibited an adhesive wetting behavior (i.e., the water droplet adhered to the surface even at 180° tilt). The OCA using hexadecane, on the contrary, decreased precipitously with increasing number of abrasion cycles. After 100 abrasion cycles, the OCA decreased from 155° to 116°, and further decreased to 70° after 350 cycles. SEM analysis was used to provide greater insight into changes in surface morphology of the abraded surfaces, and consequently the observed changes in wetting properties. Figure 9b–f show representative SEM images of the F_9PETMP(30)/SiO_2(30) films following 0, 100, 150, 200, and 350 abrasion cycles. The SEM images indicate that the initial damage to the surface occurs by removal of the fine, raspberry-like microstructure present in the as-fabricated film (Figure 9f) revealing a more course microstructure with large agglomerates after 100–150 abrasion cycles. 200 abrasion cycles results in the removal of most of the large agglomerates. Nonetheless, the abraded surface with 200 abrasion cycles retains sufficient hierarchical structure by exposing nanoparticles beneath the defects (see SEM images in Figure S4 in the Supporting Information) and is still capable of supporting a superhydrophobic wetting state. At 350 abrasion cycles, large defects are observed in the thiol–ene resin that possibly expose the substrate surface resulting in a WCA below 150° and an adhesive wetting behavior as previously described. Maintaining a superoleophobic wetting state upon multiple abrasion cycles is more challenging due to the low surface tension of the hexadecane probe liquid and a more critical dependence on the re-entrant curvature of the surface morphology. In the present work, we postulate that the rapid decrease in the OCA upon abrasion can be attributed to damage to the hierarchical, corpuscular morphology and the removal of the surface-enriched fluorinated region of the thiol–ene resin, two factors that work synergistically to yield the oil wetting behavior observed in Figure 9a.

The durability of the thiol–ene superamphiphobic surfaces toward long-term impact of water droplets was evaluated by water droplet impact measurements, an evaluation that can mimic exposure to raindrop impacts commonly encountered in outdoor coatings applications. Penetration of the hierarchical protrusions on the superamphiphobic films is expected during the drop impact event, and the occurrence increases with drop height because of the high instantaneous pressure exerted on the surface.[62] Thus, resistance to drop penetration can provide a measure of robustness for superhydrophobic and superamphiphobic surface. The drop impact measurement was conducted according to a previously reported method.[21] The details of the setup are described in the Experimental Section and illustrated in Figure S1 in the Supporting Information. Water drops were repeatedly impinged on the surface of the films from a height of 2.5 and 20 cm. For drops released from h = 2.5 cm (impact velocity of 0.7 m/s), the F_9PETMP(30)/SiO_2(30) films did not show any sign of water drop penetration even after extended testing (the experiment was ended after 7600 impact events) indicating a robust superhydrophobic wetting state. For drops released from h = 20 cm (impact velocity of 1.98 m/s), drop penetration and adhesion to film was observed after 4160 drop impact events, coating superhydrophobic properties degrade.

The stability of the cross-linked thiol–ene coatings and of the associated superamphiphobic wetting behavior was further assessed by exposure of the samples to a variety of environmental conditions, including variations in temperature and pH. F_9PETMP(30)/SiO_2(30) samples were exposed to 120 °C in an air circulation oven to evaluate the elevated temperature stability of the films. As shown in Figure 10, the static water and oil (hexadecane) contact angles were fairly constant over a 24 h exposure period at 120 °C illustrating the

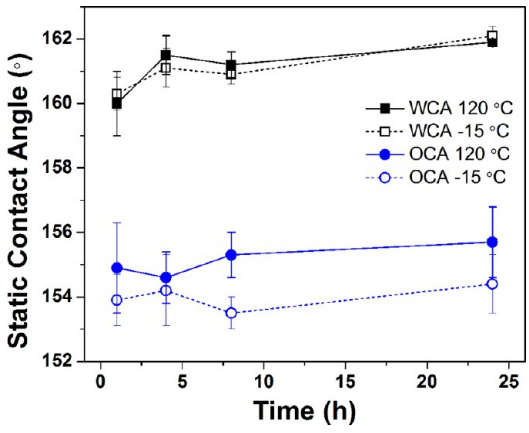

Figure 10. Static water and oil contact angles versus exposure time at −15 and 120 °C for the F_9PETMP(30)/SiO_2(30) surface. The error bars represent one standard deviation of the data, which is taken as the uncertainty of the measurement.

thermal stability of the microstructure−stability that can be attributed to the highly cross-linked thiol−ene polymer matrix resulting from photopolymerization. Likewise, the F_9PETMP-(30)/SiO_2(30) samples were exposed to subfreezing temperatures (−15 °C), and again, the static water and oil contact angles showed minimal changes over a 24 h exposure period. The chemical stability of the F_9PETMP(30)/SiO_2(30) films was evaluated by complete submersion of the samples into ambient temperature aq. H_2SO_4 (pH 2) and aq. KOH (pH 12) solutions for 24 h. As shown in Figure 11, the static water contact angles remained above 160° after 24 h in acid or base, whereas the oil contact angles remained above 155° under the same conditions.

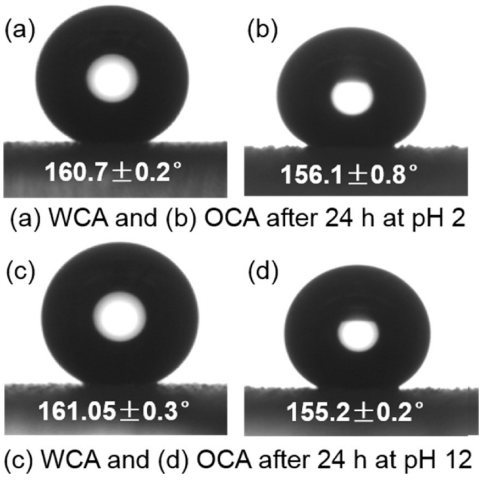

Figure 11. (a) Static water and (b) oil contact angles for F_9PETMP(30)/SiO_2(30) after immersion in aqueous H_2SO_4 (pH 2) for 24 h. (c) Static water and (d) oil contact angles for F_9PETMP(30)/SiO_2(30) after immersion in aqueous KOH (pH 12) for 24 h.

4. CONCLUSIONS

In this paper, we have demonstrated a simple, fast, and scalable approach to fabricate superamphiphobic coatings via spray deposition and UV photopolymerization of hydrophobic nanoparticle-laden thiol−ene resins containing a fluorinated multifunctional thiol. Atomization of the nanoparticle-containing resin resulted in the deposition of films with a multiscale, corpuscular morphology exhibiting both micro- and nanometer-scale roughness. Surface segregation of the fluorinated thiol provided an interface with sufficiently low surface energy that, when combined with the hierarchically rough morphology, resulted in coatings with water and oil contact angles above 150° and contact angle hysteresis values below 10° for the best performing formulations. As expected, formulations containing the longer perfluorinated chain in F_9PETMP provided better antiwetting performance than the shorter F_6PETMP formulation with low surface tension liquids, although superamphiphobicity was achieved with the F_6PETMP(30)/SiO_2(30) system. The facile nature of the spray deposition and photopolymerization process enables the preparation of superamphiphobic coatings on a variety of substrates, including textiles, in a rapid and scalable manner. Photopolymerization of the thiol−ene matrix provided superamphiphobic coatings with robust antiwetting behavior following exposure to acidic (pH 2) and basic (pH 12) solutions, and after extended exposure to subfreezing (−15 °C) and elevated temperatures (120 °C). The F_9PETMP(30)/SiO_2(30) coatings displayed a robust response in terms of maintaining superhydrophobicity following multiple mechanical abrasion cycles; however, the superoleophobic wetting properties degraded rather quickly following mechanical damage to the surface. The mechanical durability of the delicate surface structure necessary to maintain superamphiphobicity continues to be a challenge and a potential barrier for broader implementation of antiwetting technologies. Current and ongoing efforts in our lab continue to address these challenges using simple and scalable fabrication approaches.

■ ASSOCIATED CONTENT

Supporting Information

Additional information regarding abrasion and drop impact testing, XPS analysis, wetting behavior of the surfaces, and video files showing interactions of water and hexadecane with the surfaces. This material is available free of charge via the Internet at http://pubs.acs.org.

■ AUTHOR INFORMATION

Corresponding Author

*E-mail: derek.patton@usm.edu.

Author Contributions

The manuscript was written through contributions of all authors. All authors have given approval to the final version of the manuscript.

Funding

Hannele Heusser contributed to this work as a high school student (Oak Grove High School, Hattiesburg, MS) during a summer internship in the Patton Research Lab.

Notes

The authors declare no competing financial interest.

■ ACKNOWLEDGMENTS

This work was supported by the National Science Foundation (DMR-1041853 and CAREER Award DMR-1056817). B.S. acknowledges the U.S. Department of Education GAANN Fellowship Program (Award P200A120118) for financial support.

■ REFERENCES

(1) Butt, H.-J.; Graf, K.; Kappl *Physics and Chemistry of Interfaces*, 2nd ed.; Wiley-VCH: Weinheim, Germany, 2006.
(2) Barthlott, W.; Neinhuis, C. Purity of the Sacred Lotus, or Escape from Contamination in Biological Surfaces. *Planta* **1997**, *202*, 1−8.
(3) Hensel, R.; Helbig, R.; Aland, S.; Voigt, A.; Neinhuis, C.; Werner, C. Tunable Nano-Replication to Explore the Omniphobic Characteristics of Springtail Skin. *NPG Asia Mater.* **2013**, *5*, e37.
(4) Helbig, R.; Nickerl, J.; Neinhuis, C.; Werner, C. Smart Skin Patterns Protect Springtails. *PLoS One* **2011**, *6*, e25105.
(5) Wenzel, R. N. Resistance of Solid Surfaces to Wetting by Water. *Ind. Eng. Chem.* **1936**, *28*, 988−994.
(6) Cassie, A. B. D.; Baxter, S. Wettability of Porous Surfaces. *Trans. Faraday Soc.* **1944**, *40*, 546−551.
(7) Feng, X.; Jiang, L. Design and Creation of Superwetting/Antiwetting Surfaces. *Adv. Mater.* **2006**, *18*, 3063−3078.
(8) Li, X.-M.; Reinhoudt, D.; Crego-Calama, M. What Do We Need for a Superhydrophobic Surface? A Review on the Recent Progress in the Preparation of Superhydrophobic Surfaces. *Chem. Soc. Rev.* **2007**, *36*, 1350−1368.

(9) Roach, P.; Shirtcliffe, N. J.; Newton, M. I. Progess in Superhydrophobic Surface Development. *Soft Matter* **2008**, *4*, 224−240.
(10) Sun, T. L.; Feng, L.; Gao, X. F.; Jiang, L. Bioinspired Surfaces with Special Wettability. *Acc. Chem. Res.* **2005**, *38*, 644−652.
(11) Epstein, A. K.; Pokroy, B.; Seminara, A.; Aizenberg, J. Bacterial Biofilm Shows Persistent Resistance to Liquid Wetting and Gas Penetration. *Proc. Natl. Acad. Sci. U.S.A.* **2010**, DOI: doi: 10.1073/pnas.1011033108.
(12) Hensel, R.; Helbig, R.; Aland, S.; Braun, H.-G.; Voigt, A.; Neinhuis, C.; Werner, C. Wetting Resistance at Its Topographical Limit: The Benefit of Mushroom and Serif T Structures. *Langmuir* **2013**, *29*, 1100−1112.
(13) Bellanger, H.; Darmanin, T.; Taffin de Givenchy, E.; Guittard, F. Chemical and Physical Pathways for the Preparation of Superoleophobic Surfaces and Related Wetting Theories. *Chem. Rev.* **2014**, *114*, 2694−2716.
(14) Tuteja, A.; Choi, W.; Ma, M.; Mabry, J. M.; Mazzella, S. A.; Rutledge, G. C.; McKinley, G. H.; Cohen, R. E. Designing Superoleophobic Surfaces. *Science* **2007**, *318*, 1618−1622.
(15) Tuteja, A.; Choi, W.; Mabry, J. M.; McKinley, G. H.; Cohen, R. E. Robust Omniphobic Surfaces. *Proc. Natl. Acad. Sci. U.S.A.* **2008**, *105*, 18200−18205.
(16) Xue, Z.; Liu, M.; Jiang, L. Recent Developments in Polymeric Superoleophobic Surfaces. *J. Polym. Sci., Part B: Polym. Phys.* **2012**, *50*, 1209−1224.
(17) Butt, H.-J.; Semprebon, C.; Papadopoulos, P.; Vollmer, D.; Brinkmann, M.; Ciccotti, M. Design Principles for Superamphiphobic Surfaces. *Soft Matter* **2013**, *9*, 418−428.
(18) Liu, K.; Tian, Y.; Jiang, L. Bio-inspired Superoleophobic and Smart Materials: Design, Fabrication, and Application. *Prog. Mater. Sci.* **2013**, *58*, 503−564.
(19) Chu, Z.; Seeger, S. Superamphiphobic Surfaces. *Chem. Soc. Rev.* **2014**, *43*, 2784−2798.
(20) Ahuja, A.; Taylor, J. A.; Lifton, V.; Sidorenko, A. A.; Salamon, T. R.; Lobaton, E. J.; Kolodner, P.; Krupenkin, T. N. Nanonails: A Simple Geometrical Approach to Electrically Tunable Superlyophobic Surfaces. *Langmuir* **2007**, *24*, 9−14.
(21) Deng, X.; Mammen, L.; Butt, H.-J.; Vollmer, D. Candle Soot as a Template for a Transparent Robust Superamphiphobic Coating. *Science* **2012**, *335*, 67−70.
(22) Paven, M.; Papadopoulos, P.; Mammen, L.; Deng, X.; Sachdev, H.; Vollmer, D.; Butt, H.-J. Optimization of Superamphiphobic Layers Based on Candle Soot. *Pure Appl. Chem.* **2014**, *86*, 87−96.
(23) Liu, X.; Wu, W.; Wang, X.; Luo, Z.; Liang, Y.; Zhou, F. A Replication Strategy for Complex Micro/Nanostructures with Superhydrophobicity and Superoleophobicity and High Contrast Adhesion. *Soft Matter* **2009**, *5*, 3097−3105.
(24) Ghosh, N.; Bajoria, A.; Vaidya, A. A. Surface Chemical Modification of Poly(dimethylsiloxane)-Based Biomimetic Materials: Oil-Repellent Surfaces. *ACS Appl. Mater. Interfaces* **2009**, *1*, 2636−2644.
(25) Ganesh, V. A.; Dinachali, S. S.; Nair, A. S.; Ramakrishna, S. Robust Superamphiphobic Film from Electrospun TiO2 Nanostructures. *ACS Appl. Mater. Interfaces* **2013**, *5*, 1527−1532.
(26) Jiang, W.; Grozea, C. M.; Shi, Z.; Liu, G. Fluorinated Raspberry-like Polymer Particles for Superamphiphobic Coatings. *ACS Appl. Mater. Interfaces* **2014**, *6*, 2629−2638.
(27) Leng, B.; Shao, Z.; de With, G.; Ming, W. Superoleophobic Cotton Textiles. *Langmuir* **2009**, *25*, 2456−2460.
(28) He, Z.; Ma, M.; Lan, X.; Chen, F.; Wang, K.; Deng, H.; Zhang, Q.; Fu, Q. Fabrication of a Transparent Superamphiphobic Coating with Improved Stability. *Soft Matter* **2011**, *7*, 6435−6443.
(29) Wang, H.; Xue, Y.; Lin, T. One-Step Vapour-Phase Formation of Patternable, Electrically Conductive, Superamphiphobic Coatings on Fibrous Materials. *Soft Matter* **2011**, *7*, 8158−8161.
(30) Wang, H.; Zhou, H.; Gestos, A.; Fang, J.; Niu, H.; Ding, J.; Lin, T. Robust, Electro-Conductive, Self-Healing Superamphiphobic Fabric Prepared by One-Step Vapour-Phase Polymerisation of Poly(3,4-ethylenedioxythiophene) in the Presence of Fluorinated Decyl Polyhedral Oligomeric Silsesquioxane and Fluorinated Alkyl silane. *Soft Matter* **2013**, *9*, 277−282.
(31) Yang, J.; Zhang, Z.; Xu, X.; Men, X.; Zhu, X.; Zhou, X. Superoleophobic Textured Aluminum Surfaces. *New J. Chem.* **2011**, *35*, 2422−2426.
(32) Jin, H.; Tian, X.; Ikkala, O.; Ras, R. H. A. Preservation of Superhydrophobic and Superoleophobic Properties upon Wear Damage. *ACS Appl. Mater. Interfaces* **2013**, *5*, 485−488.
(33) Zhou, H.; Wang, H.; Niu, H.; Gestos, A.; Lin, T. Robust, Self-Healing Superamphiphobic Fabrics Prepared by Two-Step Coating of Fluoro-Containing Polymer, Fluoroalkyl Silane, and Modified Silica Nanoparticles. *Adv. Funct. Mater.* **2013**, *23*, 1664−1670.
(34) Steele, A.; Bayer, I.; Loth, E. Inherently Superoleophobic Nanocomposite Coatings by Spray Atomization. *Nano Lett.* **2008**, *9*, 501−505.
(35) Das, A.; Schutzius, T. M.; Bayer, I. S.; Megaridis, C. M. Superoleophobic and Conductive Carbon Nanofiber/Fluoropolymer Composite Films. *Carbon* **2012**, *50*, 1346−1354.
(36) Srinivasan, S.; Chhatre, S. S.; Mabry, J. M.; Cohen, R. E.; McKinley, G. H. Solution Spraying of Poly(Methyl Methacrylate) Blends to Fabricate Microtextured, Superoleophobic Surfaces. *Polymer* **2011**, *52*, 3209−3218.
(37) Yang, J.; Zhang, Z.; Men, X.; Xu, X.; Zhu, X. A Simple Approach to Fabricate Superoleophobic Coatings. *New J. Chem.* **2011**, *35*, 576−580.
(38) Wang, X.; Hu, H.; Ye, Q.; Gao, T.; Zhou, F.; Xue, Q. Superamphiphobic Coatings with Coralline-Like Structure Enabled by One-Step Spray of Polyurethane/Carbon Nanotube Composites. *J. Mater. Chem.* **2012**, *22*, 9624−9631.
(39) Campos, R.; Guenthner, A. J.; Meuler, A. J.; Tuteja, A.; Cohen, R. E.; McKinley, G. H.; Haddad, T. S.; Mabry, J. M. Superoleophobic Surfaces through Control of Sprayed-on Stochastic Topography. *Langmuir* **2012**, *28*, 9834−9841.
(40) Ge, B.; Zhang, Z.; Men, X.; Zhu, X.; Zhou, X. Sprayed Superamphiphobic Coatings on Copper Substrate with Enhanced Corrosive Resistance. *Appl. Surf. Sci.* **2014**, *293*, 271−274.
(41) Tiwari, M. K.; Bayer, I. S.; Jursich, G. M.; Schutzius, T. M.; Megaridis, C. M. Highly Liquid-Repellent, Large-Area, Nanostructured Poly(vinylidene fluoride)/Poly(ethyl 2-cyanoacrylate) Composite Coatings: Particle Filler Effects. *ACS Appl. Mater. Interfaces* **2010**, *2*, 1114−1119.
(42) Xiong, D.; Liu, G.; Scott Duncan, E. J. Robust Amphiphobic Coatings from Bi-Functional Silica Particles on Flat Substrates. *Polymer* **2013**, *54*, 3008−3016.
(43) Sparks, B. J.; Hoff, E. F. T.; Xiong, L.; Goetz, J. T.; Patton, D. L. Superhydrophobic Hybrid Inorganic−Organic Thiol-ene Surfaces Fabricated via Spray-Deposition and Photopolymerization. *ACS Appl. Mater. Interfaces* **2013**, *5*, 1811−1817.
(44) Shin, J.; Nazarenko, S.; Hoyle, C. E. Effects of Chemical Modification of Thiol−Ene Networks on Enthalpy Relaxation. *Macromolecules* **2009**, *42*, 6549−6557.
(45) Goetz, J.; Kwisnek, L.; Nazarenko, S. From Gas Barriers to High Gas Flux Membranes: UV-Cured Thiol-ene Networks for Transport Applications. *RadTech Report* **2012**, *27*, 27−32.
(46) Fowkes, F. M. Attractive Forces at Interfaces. *Ind. Eng. Chem.* **1964**, *56*, 40−52.
(47) Seah, M. P.; Dench, W. A., Quantitative Electron Spectroscopy of Surfaces: A Standard Data Base for Electron Inelastic Mean Free Paths in Solids. In *Surf. Interface Anal.***1979**; Vol. *1*, pp 2−11.
(48) Zhu, X.; Zhang, Z.; Yang, J.; Xu, X.; Men, X.; Zhou, X. Facile Fabrication of a Superhydrophobic Fabric with Mechanical Stability and Easy-Repairability. *J. Colloid Interface Sci.* **2012**, *380*, 182−186.
(49) Yeong, Y. H.; Davis, A.; Steele, A.; Loth, E.; Bayer, I. S., Spray Deposition Effects on Superhydrophobicity and Durability of Nanocoatings. *Surf. Innovations* **2014**, Ahead of Print 10.1680/si.13.00044.
(50) Mao, Y.; Gleason, K. K. Vapor-Deposited Fluorinated Glycidyl Copolymer Thin Films with Low Surface Energy and Improved Mechanical Properties. *Macromolecules* **2006**, *39*, 3895−3900.

(51) Thomas, R. R.; Anton, D. R.; Graham, W. F.; Darmon, M. J.; Sauer, B. B.; Stika, K. M.; Swartzfager, D. G. Preparation and Surface Properties of Acrylic Polymers Containing Fluorinated Monomers. *Macromolecules* **1997**, *30*, 2883−2890.
(52) Moulder, J. F.; Stickle, W. F.; Sobol, P. E.; Bomben, K. D. *Handbook of X-ray Photoelectron Spectroscopy*; Perkin-Elmer: Eden Prairie, MN, 1995.
(53) Bernett, M. K.; Zisman, W. A. Wetting Properties of Tetrafluoroethylene and Hexafluoropropylene Copolymers. *J. Phys. Chem.* **1960**, *64*, 1292−1294.
(54) Tsibouklis, J.; Graham, P.; Eaton, P. J.; Smith, J. R.; Nevell, T. G.; Smart, J. D.; Ewen, R. J. Poly(perfluoroalkyl methacrylate) Film Structures: Surface Organization Phenomena, Surface Energy Determinations, and Force of Adhesion Measurements. *Macromolecules* **2000**, *33*, 8460−8465.
(55) Kumar, V.; Pulpytel, J.; Rauscher, H.; Mannelli, I.; Rossi, F.; Arefi-Khonsari, F. Fluorocarbon Coatings Via Plasma Enhanced Chemical Vapor Deposition of 1H,1H,2H,2H-perfluorodecyl Acrylate - 2, Morphology, Wettability and Antifouling Characterization. *Plasma Processes Polym.* **2010**, *7*, 926−938.
(56) Jung, Y. C.; Bhushan, B. Mechanically Durable Carbon Nanotube Composite Hierarchical Structures with Superhydrophobicity, Self-Cleaning, and Low-Drag. *ACS Nano* **2009**, *3*, 4155−4163.
(57) Su, C.; Xu, Y.; Gong, F.; Wang, F.; Li, C. The Abrasion Resistance of a Superhydrophobic Surface Composed of Polyurethane Elastomer. *Soft Matter* **2010**, *6*, 6068−6071.
(58) Verho, T.; Bower, C.; Andrew, P.; Franssila, S.; Ikkala, O.; Ras, R. H. A. Mechanically Durable Superhydrophobic Surfaces. *Adv. Mater.* **2011**, *23*, 673−678.
(59) Huovinen, E.; Takkunen, L.; Korpela, T.; Suvanto, M.; Pakkanen, T. T.; Pakkanen, T. A. Mechanically Robust Superhydrophobic Polymer Surfaces Based on Protective Micropillars. *Langmuir* **2014**, *30*, 1435−1443.
(60) Raza, A.; Si, Y.; Wang, X.; Ren, T.; Ding, B.; Yu, J.; S. Al-Theyab, S. Novel Fluorinated Polybenzoxazine-Silica Films: Chemical Synthesis and Superhydrophobicity. *RSC Adv.* **2012**, *2*, 12804−12811.
(61) Bayer, I. S.; Fragouli, D.; Martorana, P. J.; Martiradonna, L.; Cingolani, R.; Athanassiou, A. Solvent Resistant Superhydrophobic Films from Self-Emulsifying Carnauba Wax-Alcohol Emulsions. *Soft Matter* **2011**, *7*, 7939−7943.
(62) Deng, X.; Schellenberger, F.; Papadopoulos, P.; Vollmer, D.; Butt, H.-J. Liquid Drops Impacting Superamphiphobic Coatings. *Langmuir* **2013**, *29*, 7847−7856.